The Molecular Determinants of the Increased Reduction Potential of the Rubredoxin Domain of Rubrerythrin Relative to Rubredoxin

Yan Luo,[†] Can E. Ergenekan,[‡] Justin T. Fischer,[‡] Ming-Liang Tan,[†] and Toshiko Ichiye[†*]
[†]Department of Chemistry, Georgetown University, Washington, District of Columbia; and [‡]School of Molecular Biosciences, Washington State University, Pullman, Washington

ABSTRACT Based on the crystal structures, three possible sequence determinants have been suggested as the cause of a 285 mV increase in reduction potential of the rubredoxin domain of rubrerythrin over rubredoxin by modulating the polar environment around the redox site. Here, electrostatic calculations of crystal structures of rubredoxin and rubrerythrin and molecular dynamics simulations of rubredoxin wild-type and mutants are used to elucidate the contributions to the increased reduction potential. Asn^{160} and His^{179} in rubrerythrin versus valines in rubredoxins are predicted to be the major contributors, as the polar side chains contribute significantly to the electrostatic potential in the redox site region. The mutant simulations show both side chains rotating on a nanosecond timescale between two conformations with different electrostatic contributions. Reduction also causes a change in the reduction energy that is consistent with a linear response due to the interesting mechanism of shifting the relative populations of the two conformations. In addition to this, a simulation of a triple mutant indicates the side-chain rotations are approximately anticorrelated so whereas one is in the high potential conformation, the other is in the low potential conformation. However, Ala^{176} in rubrerythrin versus a leucine in rubredoxin is not predicted to be a large contributor, because the solvent accessibility increases only slightly in mutant simulations and because it is buried in the interface of the rubrerythrin homodimer.

INTRODUCTION

The reduction potentials of electron transfer proteins determine the driving force of the electron transfer reactions in which they are involved. Iron-sulfur proteins are ubiquitous electron transfer proteins containing Fe-S sites with one to eight iron atoms (1–3). Homologous Fe-S proteins can have very different reduction potentials that span a few hundred millivolts even though the structures of the redox sites are highly similar (4,5). The simplest Fe-S site contains a single iron atom tetrahedrally coordinated by four cysteinyl thiolates, which can be referred to as a [1Fe-0S] or [1Fe] cluster. The [1Fe] cluster is found in rubredoxin, a small ($M_r \approx 6000$) electron transfer protein in bacteria and archaea (5). In addition, it is found in rubrerythrin, which was first isolated from the sulfate reducing bacteria *Desulfovibrio vulgaris* (6), and is thought to be involved in the reduction of hydrogen peroxide in anaerobic bacteria (7–9). Rubrerythrin has an N-terminal ferritin domain with an oxo-bridged diiron metal center and a C-terminal rubredoxin domain (Fig. 1) with a single [1Fe] center (10). However, the [1Fe] center in the rubredoxin domain of *D. vulgaris* rubrerythrin has a reduction potential of 230 ± 10 mV (6), compared to a range of −100 to +60 mV for the rubredoxins (11). Finding the molecular determinants of this large increase in reduction potential is important in understanding how metalloproteins tune their reduction potentials.

Structural analysis have pointed to three possible determinants in *D. vulgaris* rubrerythrin (DvRr) of the greatly increased reduction potential relative to *Clostridium pasteurianum* rubredoxin (CpRd) and four other rubredoxins (10). Two are the polar residues Asn^{160} and His^{179}, which are equivalent to Val^{8} and Val^{44} in CpRd. The placement of two polar groups near the iron center could greatly increase the reduction potential of a redox site if they are oriented around the metal center to stabilize the reduced form of the clusters. Furthermore, residue 44 has been identified as a sequence determinant of the reduction potential in rubredoxins, so a larger nonpolar Val side chain at residue 44 results in lower reduction potentials by ~50 mV relative to a smaller Ala side chain because of a backbone shift (12–14). The third possible determinant is Ala^{176}, which is equivalent to Leu^{41} in CpRd, where it acts as a water gate (15–17). The smaller Ala might increase the reduction potential by exposing the redox site more to solvent, which would increase the reduction potential.

Computational studies of reduction potentials of Fe-S proteins have generally focused on the overall reduction potentials (18–21). However, many experimental site-specific mutational studies have obtained results contrary to simple physical chemical arguments (22–24) due to a multitude of possible changes at a molecular level, and so computational studies can play an important role in identifying sequence determinants. For instance, our studies of residue 44 in the rubredoxins (12–14) showed an indirect effect of nonpolar residues on the reduction potential by causing a shift in the backbone—which is polar due to size differences of the side chains. Furthermore, these studies showed that the reduction potential was not directly

Submitted December 23, 2008, and accepted for publication November 4, 2009.

*Correspondence: ti9@georgetown.edu

Can E. Ergenekan's present address is Supercomputer Institute, University of Minnesota, Minneapolis, MN 55455.

Editor: Kathleen B. Hall.

0006-3495/10/02/0560/9 $2.00

doi: 10.1016/j.bpj.2009.11.006

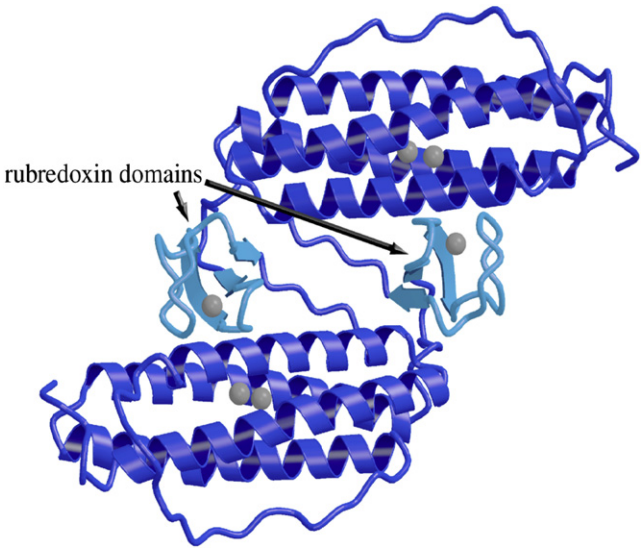

FIGURE 1 Ribbon diagram depicting the Dv (1LKM) rubrerythrin homodimer in blue, with the metal atoms for the diiron site and the $Fe(S)_4$ site shown as gray van der Waals spheres.

proportional to the size of the side chain. In particular, although a change from Val to Ala increased the potential by ~50 mV, a change from Ala to Gly only caused a slight change because the backbone could no longer shift and a change from Val to Leu also only caused a slight change because the extra atoms of the Leu were accommodated within cavities of the protein.

From a computational standpoint, our earlier studies indicate that electrostatic calculations using high-resolution x-ray crystallographic structures combined with bioinformatics sequence analysis (25,26) can, in some cases, give a better answer than molecular dynamics (MD) simulations. Therefore, assessing the relative accuracy is important, as many researchers do not have access to computational resources for multi-nanosecond scale MD simulations for simple screening of potential mutants. In computational studies of rubredoxins (12), which have been experimentally verified (13,15,27), and ferredoxins (28), which have also been experimentally verified (29–31), sequence determinants involve changes in distance of <0.5 Å of polar groups hydrogen-bonded to the cluster and changes in energy of 50–100 meV. In particular, sequence determinant(s) of changes between homologous proteins can be difficult to identify as they may involve small changes mixed with many other irrelevant changes. For these types of studies, high-resolution x-ray crystal structures are generally more reliable than the structures in MD simulations, which are dependent on the potential energy function. Moreover, although Poisson or Poisson-Boltzmann continuum electrostatic calculations can give accurate predictions of total reduction potentials, contributions of sequence determinants that are hydrogen-bonded directly to the cluster are sensitive to the grid size and dielectric boundary definition. For instance, Poisson-Boltzmann calculations of Fe-S proteins have used a vacuum dielectric for the cluster and nearby residues (20), so that using Coulomb's law and interatomic distances for the contribution of nearby residues is more accurate than a grid-based solution. On the other hand, MD simulations are useful in studying site-specific mutants once sequence determinants have been identified, particularly in identifying factors such as backbone flexibility (32), alternate conformations (which must be explicitly added in an x-ray structure determination (33)), and transient water penetration.

An important issue in reconciling the accuracy of the previous studies of reduction potentials by x-ray structure analyses of rubredoxins (12) and ferredoxin (28) with more recent studies by MD (21,34,35) is that the x-ray analyses assume that the hydrogen-bonded groups acted as permanently polarized dipoles, whereas MD studies generally assume that polar groups will respond linearly to the change in charge upon reduction—ultimately leading to differences of a factor of 1/2 in the reduction potential (see Methods). Generally, the validity of the linear response approximation has been an important issue for proteins (36), and whereas a simple polar solvent will have a linear response, proteins appear to have a permanent component in the polarization that would still be present at zero charge in addition to the linear response to the charge of the redox site (37), which may be similar to Warshel's preorganization concept (38). Here, we examine the linearity of the response of specific residues rather than the entire protein in comparisons of x-ray structures of homologous proteins and multi-nanosecond MD simulations of mutants. The work presented here utilizes methods developed earlier (12–15) to elucidate the individual contributions of these possible determinants to the increased reduction potential of the rubredoxin domain of rubrerythrin over that of rubredoxin from analysis of crystal structure of wild-type (wt) DvRr and CpRd, as well as MD simulations of wt and mutant rubredoxins. Specifically, the aim is to examine the effects of mutation to asparagine, histidine, and alanine as found in DvRr in the equivalent positions of CpRd, and to relate these results to differences between DvRr and CpRd in their experimental reduction potentials. For convenience, the sequence numbering of CpRd is used for the equivalent position of DvRr, such that Asn^{160}, His^{179}, and Ala^{176} are referred to as Asn^{8}, His^{44}, and Ala^{41}, respectively.

METHODS

Crystal structure and bioinformatics analysis

The crystal structures of oxidized [1FHH at 1.50 Å resolution (16)] and reduced [1FHM at 1.50 Å resolution (16)] CpRd, oxidized [1SMM at 1.36 Å resolution (15)] and reduced [1SMU at 1.43 Å resolution (15)] L41A CpRd, and oxidized [1LKM at 1.69 Å resolution (39)] and reduced [1LKO at 1.63 Å resolution (39)] DvRr were obtained from the Brookhaven Protein Data Bank (40). The hydrogen positions were built for all polar

hydrogens using the HBUILD facility of CHARMM 25 (41) followed by 100 steps of steepest descent minimization of the entire protein. In the DvRr crystal structures, the oxygen and nitrogen positions of Asn^{160} were switched so that the nitrogen formed a hydrogen bond to the iron site as reported in an earlier structure (42).

Sequence analysis was performed using BLAST (43). Forty-two rubrerythrins were obtained from the SWISSPROT and TrEMBL (44) databases and forty-two rubredoxins were obtained from the SWISSPROT database.

Molecular-dynamics simulations

Molecular dynamics (MD) simulations of the wt CpRd and four CpRd mutants (described below) were performed with the molecular mechanics and dynamics program package CHARMM 29 (41), beginning with the 5RXN at 1.20 Å resolution (45) crystal structure, along with crystal waters. The Verlet algorithm was used with a time step of 0.001 ps in the microcanonical-ensemble at a temperature of ~300 K. Truncated rectangular-octahedral periodic boundary conditions were used. The potential energy function used the parameters of CHARMM 19 (41), TIP3P for water (46) and additional parameters for the ions and the iron-sulfur site (17), in which nonpolar hydrogens were treated implicitly using the extended atom method. All bonds containing hydrogens were constrained to their equilibrium bond lengths using the SHAKE algorithm (47). Long-range forces were switched smoothly to zero using an atom-based force-switch method (48) between 10 Å and 14 Å and the nonbonded and image atom lists were updated heuristically using a cutoff distance of 15 Å. This method was used to maintain consistency with earlier studies; the short-range nature of the dipole interaction makes this method reasonable here.

The initial wt oxidized and reduced systems were prepared as described in previous work (14), consisting of energy minimization and solvation of the crystal structure (protein plus crystal waters), followed by 62 ps of solvent equilibration. The initial wt oxidized system consisted of 501 protein atoms, 1835 water molecules, 15 sodium ions, and five chlorine ions, whereas the initial wt reduced system, which was also constructed from the oxidized crystal structure, consisted of 501 protein atoms, 1834 water molecules, 16 sodium ions, and five chlorine ions. Structures of the oxidized and reduced mutant forms of CpRd, Val^{8} to asparagine (V8N CpRd), Val^{44} to histidine (V44H CpRd), Leu^{41} to alanine (L41A CpRd), and the triple mutant (triple CpRd), were constructed from the initial oxidized and reduced wt systems respectively, by using QUANTA (49) as described in earlier work (14). However, the crystal structure of DvRr (1RYT) 1RYT at 2.10 Å resolution (10) was used to determine the initial starting conformation of the dihedral angles for the mutated residues.

MD simulations were carried out starting from the oxidized and reduced wt and mutant systems. The systems were equilibrated by molecular dynamics, scaling the velocities every 0.2 ps until 10 ps after the last scale for a total of 15 ps to 25 ps, followed by 920 ps unperturbed. After equilibration, the systems were propagated for 5 ns and analysis utilized coordinates at 0.01 ps intervals from this 5 ns.

Electrostatic calculations

The electrostatic interactions of the sequence determinants with the iron site are calculated as described in previous work (12,28), and may be related to the reduction potential as follows (26). The free energy change upon reduction ΔG is related to the reduction potential E° by the Nernst equation,

$$-n\Im E^{\circ} = \Delta G, \tag{1}$$

where $\Im$ is Faraday's constant and n is the number of electrons transferred. Furthermore, the free energy of each state can be obtained from the electrostatic energy E_e between the redox site and the environment of each state from the thermodynamic integration as the major change is in the electrostatics (37) and the self-energy terms cancel for mutants. In the two extremes, if the environmental response is linear with charge, the free energy should equal to half of the energy $\Delta G = 1/2\ \Delta E_e$, whereas, if the electrostatic potential in the redox site region is a permanent potential independent of charge (37), the free energy is equal to the energy $\Delta G = \Delta E_e$. To focus on a specific sequence determinant, the contribution of residue k to the electrostatic energy is

$$E_e(k) = \sum_{i=\text{redox site atoms}} \sum_{j=\text{atoms of residue } k} \frac{q_i Q_j}{r_{ij}}, \tag{2}$$

where q_i is the charge of atom i of the redox site, Q_j is the charge of atom i of residue k, and r_{ij} is the distance between atoms i and j. Thus, the reduction energy is

$$\Delta E(k) = \langle E_e(k)\rangle_{red} - \langle E_e(k)\rangle_{oxd}. \tag{3}$$

For the crystal structure calculations, it denotes a calculation using the structure in the state α where α = oxd; whereas for the MD simulations, $\langle\ldots\rangle_\alpha$ denotes a time average in the state α. Furthermore, the energy gap is

$$\Delta V(k) = \sum_{i=\text{redox site atoms}} \sum_{j=\text{atoms of residue } k} \frac{\Delta q_i Q_j}{r_{ij}}, \tag{4}$$

where Δq_i is the change in charge of atom i upon reduction and the other variables are as in Eq. 2. If the system responds linearly, the free energy is then given by (25,36,50,51)

$$\Delta G(k) = \frac{1}{2}\left[\langle \Delta V(k)\rangle_{red} + \langle \Delta V(k)\rangle_{oxd}\right]. \tag{5}$$

Note that a linear response means a purely linear dependence on the charge, with no constant term corresponding to a permanent polarization.

To examine the linearity of the environmental response in the MD simulations, the previously proposed (37) linear-polarization measure

$$\xi^{(1)}_{q_{oxd}q_{red}} = \frac{\langle\phi\rangle_{red}/q_{red}}{\langle\phi\rangle_{oxd}/q_{oxd}} \tag{6}$$

is also calculated, where ϕ is the electrostatic potential at an ion. The linearity of the response potential with respect to the applied field (i.e., the redox site charge) can be demonstrated from continuum electrostatics (52). Note that

$$\xi^{(1)}_{q_{oxd}q_{red}} = 1$$

implies that the potentials are consistent with a linear response, whereas

$$\xi^{(1)}_{q_{oxd}q_{red}} = q_{oxd}/q_{red}$$

implies that the potentials are consistent with a permanent polarization; of course, other phenomena may give rise to the same values as only the initial and final states are compared. Because here the change in charge is delocalized over several atoms in the redox site, the contributions of residue k to the electrostatic potential at the redox site is approximated as $-n\Im\langle\phi\ (k)\rangle_\alpha \approx \langle\Delta V(k)\rangle_\alpha$; in other words, as an average over the redox site weighted by the charge change at each atom. Therefore, the value of ϕ for a particular redox state depends on the process being considered.

Solvent accessibility

The solvent accessibility of the redox site was calculated as the solvent contact surface area (SCSA) of the nine atoms of the redox site; namely, the iron plus the C_β and S_γ of residues 6, 9, 39, and 42, which are the cysteinyl ligands of the iron site. In practice, the only atoms of the redox site with nonzero values of SCSA are the C_β of residue 9 and residue 42. Lee and Richard's algorithm (53) was used with a probe radius of 1.6 Å. The water penetration of the protein in the simulations is qualitatively described by the number of waters that are found in the first shell of water near the iron of the redox site, which is defined as the number of water oxygens within 6 Å from the iron.

RESULTS AND DISCUSSION

Here, two separate but related questions are addressed:

1. What are the sequence determinants of the 285 mV higher reduction potential of DvRr relative to CpRd?
2. What are the structural determinants of differences in reduction potential between V8N, L41A, V44H, triple, and wt CpRd?

Because of differences in the environment around each side chain of the two proteins and the coupling between residues 8, 41, and 44, the individual contributions of each residue difference between DvRr and CpRd may not equal the differences due to each site-specific mutation.

Identification of sequence determinants

Because structural analysis has previously pointed to residues 8, 41, and 44 as possible determinants of the difference in reduction potential between the rubrerythrins and rubredoxins (10), here these possibilities were evaluated using our general strategy for identifying sequence determinants from homologous proteins via bioinformatics sequence and electrostatic crystal structure analysis (25,26). As noted before, sequence determinants that separate homologous proteins into different classes based on their reduction potentials tend to be conserved within each reduction potential class, but differ between the classes. The sequence analysis of 42 rubrerythrins and 42 rubredoxins supported residues 8, 41, and 44 as likely determinants (Fig. S1 in the Supporting Material). Residues 8 and 44 were almost completely conserved as an Asn and a His, respectively, in the rubrerythrins, whereas they were 81% and 95%, respectively, nonpolar residues in the rubredoxins. Residue 44 was 88% Ala in rubrerythrins whereas it was either a polar residue or a larger nonpolar residue in the rubredoxins.

The oxidized and reduced crystal structures of the rubredoxin domain of DvRr (1LKM and 1LKO, respectively), CpRd (1FHH and 1FHM, respectively), and L41A CpRd (1SMM and 1SMU, respectively) were analyzed for differences in structure and energetics. Overall, the DvRr oxidized and reduced structures had a total root mean-square deviation (RMSD) of 0.24 Å and did not exhibit any significant changes near the [1Fe] center, whereas the CpRd structures had a total RMSD of 0.80 Å and exhibited small differences mainly around residue 41, which is involved in water-gating of the redox center (16).

By examining the differences in the reduction energy due to residues 8, 41, and 44 in the DvRr versus CpRd crystal structures (Table 1), the major contributions appeared to be due to the polar side chains of Asn^{8} and His^{44} in DvRr. Moreover, despite the differences in side chain sizes, there did not appear to be significant backbone shifts (Fig. 2), unlike what was found previously for other mutations of Val^{44} in CpRd (12–14). Thus, backbone contributions were small for the nonpolar residues where they are the only contribution (Table 1) and ranged from only −4 to −19 mV for the polar residues. Using the assignment of the N and O by Sieker et al. (42), the DvRr Asn8 side chain had $\chi_2 \approx 60°$ and formed a hydrogen bond to the redox site in both oxidation states, thus increasing $-\Delta E/n\Im$ relative to the wt CpRd Val^{8} by 352 mV; however, using the assignment of Jin et al. (39), it had $\chi_2 \approx -120°$, thus decreasing $-\Delta E/n\Im$ by 169 mV. Because distinguishing the N and O is difficult in an electron density map, the assignment of Sieker's group with a hydrogen bond between the NH_2 and the redox center appears reasonable (see methods). The DvRr His^{44} side chain had $\chi_2 \approx 57°$ and was oriented away from the redox site, with a hydrogen bond to the backbone carbonyl of the fourth cysteinyl ligand, thus increasing $-\Delta E/n\Im$ relative to wt CpRd Val^{44} by 160 mV. Finally, Ala^{41} in DvRr and L41A CpRd made insignificant changes in $-\Delta E/n\Im$ relative to Leu^{41} of wt CpRd.

TABLE 1 Differences of DvRr and mutant CpRd relative to wt CpRd (absolute numbers given in parentheses) in reduction energy calculated from crystal structures and experimental reduction potentials (in mV)

Protein	$-\Delta\Delta E(8)/n\Im$	$-\Delta\Delta E(41)/n\Im$	$-\Delta\Delta E(44)/n\Im$	TOTAL	$\Delta E°$(exp)*
(CpRd)	(364)	(362)	(48)	NA	(−55)
DvRr (+)†	352	30	160	542	285 ± 10
DvRr (−)†	−169	30	183	21	285 ± 10
CpRd L41A	−23	−19	14	−29	50

*Reduction potentials for CpRd (22), DvRr (6,22), and L41A (15,22).
†The "+" denotes $\chi_2 \approx 60°$ whereas "−" denotes $\chi_2 \approx -120°$ for Asn.

The SCSA of the redox site in CpRd increased from 7.8 $Å^2$ to 13.2 $Å^2$ upon reduction because of the gating behavior of Leu^{41}. However, the SCSA of the redox site in

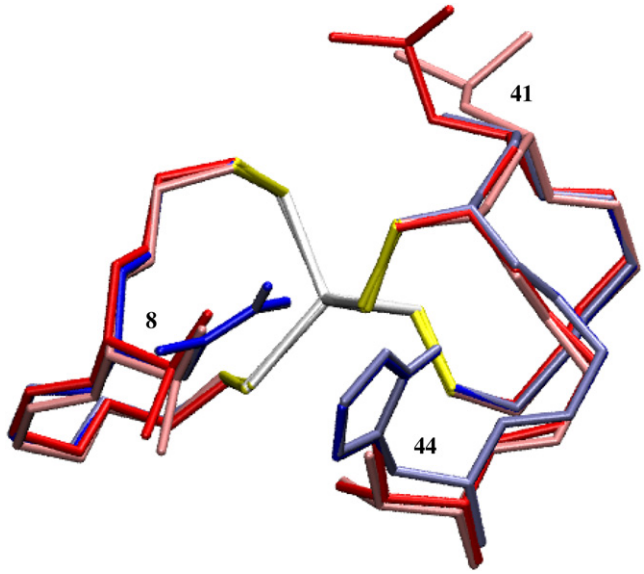

FIGURE 2 Superposition of the DvRr in oxidized (1LKM) and reduced (1LKO) states (*blue* and *ice blue*) and CpRd in oxidized (1FHH) and reduced (1FHM) states (*red* and *pink*) near the $Fe(S)_4$ metal center (*white* and *yellow*), aligned on the $Fe(S)_4$ center.

CpRd L41A changed only slightly upon reduction (~12.4 Å^2 and ~13.0 Å^2 in oxidized and reduced state, respectively). The SCSA of the redox site in DvRr monomer was 11.0 Å^2 for both the oxidized and reduced crystal structures, larger than that of the oxidized CpRd but less than that of the reduced CpRd. In the crystal structure alignment (Fig. 2), DvRr Ala^{41} (both oxidized and reduced structures) covers the redox site less than Leu^{41} does in the open gate state of oxidized CpRd but more than Leu^{41} does in the closed gate state of reduced CpRd. Moreover, the SCSA of the redox site in the DvRr homodimer was very small in both the oxidized and reduced structures, ~0.1 Å^2 and ~0 Å^2, respectively, because the redox sites reside in the interface between the two monomers and thus are restrained from contacting water.

Overall, the results for the energy differences of DvRr were approximately twice as large as the observed differences in the reduction potential for the polar side chains, because entropic contributions are important for side chains (as seen below). To obtain more quantitative results, the free energy must be determined. If the system is linear, then $\Delta G \approx 1/2\ \Delta E$; but note also that when the free energy for the x-ray structures was calculated using Eq. 5, which assumes the system is linear, the values were almost identical to the reduction energies $\Delta G \approx \Delta E$, because the oxidized and reduced structures are almost identical. Moreover, previous studies indicate that the protein contribution of rubredoxin is nonlinear because of a permanent polarization contribution (37). To investigate the linearity and determine the free energy, MD simulations were performed as described below. However, the results here along with previous studies of the rubredoxins (12) and the ferredoxins (28) show that the bioinformatics sequence and electrostatic structural analysis are as a useful means of identifying possible sequence determinants as those that can cause energy differences. In particular, this approach is useful for identifying small structural shifts giving rise to small changes in reduction potential by finding systematic trends in multiple structures (12,28), which would be difficult to separate in MD simulations.

Mutations of sequence determinants

MD simulations were analyzed for changes in structure and energetics of V8N, V44H, and L41A CpRd from the wt CpRd. The wt CpRd simulation exhibited a backbone RMSD of 1.4 and 2.3 Å from the oxidized and reduced crystal structures, respectively, based on the backbone alignment. In addition, the differences between the mutant and wt were ~1 and ~2 Å for the oxidized and reduced average structures, indicating the mutations did not change the overall structure of the protein from the wt simulation. However, changes were apparent near the redox sites. For instance, the backbone and side chain of residue 8 of both V8N and wt CpRd shifted toward the redox site upon reduction (Fig. 3 *a*).

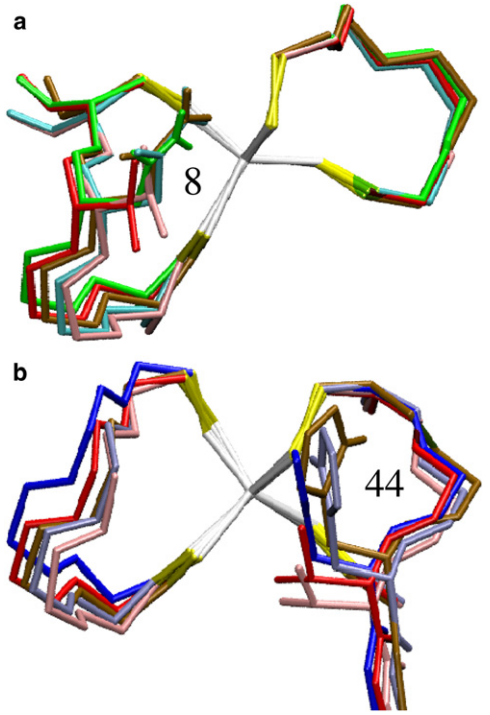

FIGURE 3 Licorice model depicting the backbone and side-chain relation interaction with the Fe(S)$_4$ center (*white* and *yellow*) of the average MD structures of (*a*) the oxidized and reduced V8N CpRd (*green* and *cyan*), the oxidized and reduced wt CpRd (*red* and *pink*), (*b*) the oxidized and reduced V44H CpRd (*blue* and *ice blue*), and the oxidized and reduced wt CpRd (*red* and *pink*). Also shown is the DvRr (1LKM) crystal structure (*ochre*). The alignment is based on the Fe(S)$_4$ center.

In addition, V44H and wt CpRd exhibited a shift in the backbone near residue 44 upon reduction and the His side chains of both oxidized and reduced states of the mutant had slightly different orientations from that in the DvRr crystal so that it no longer hydrogen-bonds to the backbone carbonyl (Fig. 3 *b*). No shift in the backbone near residue 41 between L41A and wt CpRd was observed.

The shifts in the reduction energy $-\Delta E/n\Im$ from wt CpRd calculated from MD (Table 2) were similar to the values from the x-ray structures except that the magnitude were much larger for the Asn and His (Table 1). The Asn in V8N and the triple mutant increased $-\Delta E/n\Im$ by ~580 and ~720 mV, respectively, and the His in V44H and the triple mutant increased it by ~240 and ~280 mV, respectively. However, shifts in the free energy calculated using Eq. 5 were smaller for the polar residues (Table 2) than the shifts in the energies (Table 2). In particular, the Asn in V8N and the triple mutant increased $-\Delta G/n\Im$ relative to wt by ~190 and ~160 mV, respectively, whereas the His in V44H and the triple mutant increased $-\Delta G/n\Im$ by ~180 and ~130 mV, respectively—which are in very good agreement with the experimental shifts in reduction potentials.

The difference between $-\Delta\Delta E/n\Im$ from the x-ray structures and the MD simulations for the Asn and His mutations was due to the rotation of the two polar side chains in the

TABLE 2 Differences between CpRd mutants relative wt (absolute values given in parentheses) in the reduction energy and free energy calculated from MD simulations compared to experimental reduction potentials (all in mV)

Reduction energy

Mutant	$-\Delta\Delta E(8)/n\Im$	$-\Delta\Delta E(41)/n\Im$	$-\Delta\Delta E(44)/n\Im$	TOTAL	ΔE° (exp)*
(wt)	(417)	(384)	(68)	NA	(−55)
V8N	581	10	−4	587	119
L41A	−8	29	−3	18	50
V44H	30	1	236	267	NA
Triple	716	1	284	1001	285 ± 10

Free energy

Mutant	$-\Delta\Delta G(8)/n\Im$	$-\Delta\Delta G(41)/n\Im$	$-\Delta\Delta G(44)/n\Im$	ΔE° (calc)	ΔE° (exp)*
wt	(310)	(339)	(23)	NA	(−55)
V8N	194	−6	−11	177	119
L41A	−8	−18	−0.3	−27	50
V44H	−44	4	177	137	NA
Triple	156	−2	132	286	285 ± 10

*Reduction potentials for CpRd (22),V8N (E. T. Smith, Q. Zeng, M. K. Eidsness, A. E. Burden, D.M. Kurtz, Jr., and R. A. Scott, Department of Chemistry and Center for Metalloenzyme Studies, University of Georgia, personal communication, 2002), and L41A (15,22). For the triple mutant, the value of DvRr (6,22) is given.

MD. In V8N CpRd, the Asn side chain in the oxidized state made ~15 transitions between a major conformation with ~60% population, which has $\chi_2 \approx 70^\circ$ with the NH_2 pointing toward the redox site, similar to $\chi_2 \approx 60^\circ$ for the DvRr x-ray structure (42), and a minor conformation with ~40% population, which has a $\chi_2 \approx -80^\circ$ with the NH_2 pointing into solution (Fig. S2 *a*). However, the Asn in the reduced state stayed in the $\chi_2 \approx 70^\circ$ conformation. Also, in V44H CpRd, the His side chain in the oxidized state made ~12 fairly stable transitions plus a few rapid crossings between $\chi_2 \approx 90^\circ$ with the NH toward the redox site (~85% population)—somewhat larger than $\chi_2 \approx 57^\circ$ for the DvRr x-ray structure, and $\chi_2 \approx -85^\circ$ with the NH into solution (Fig. S2 *b*). However, the His side chain in the reduced state had $\chi_2 \approx 90^\circ$ for most of the simulation, whereas at only the end of simulation the side chain flipped twice to $\chi_2 \approx -85^\circ$. Interestingly, the simulation of the triple mutant indicated that the Asn and His side chains were approximately anticorrelated so that when the Asn had $\chi_2 \approx -80^\circ$, the His had $\chi_2 \approx 90^\circ$ and when the Asn had $\chi_2 \approx 70^\circ$, the His had $\chi_2 \approx -85^\circ$, although there were two periods of ~0.8 and 0.1 ns where they were both in phase. However, only three transitions for Asn and seven for His were observed so the relative populations were not as well characterized. The electrostatic interaction energy between the two residues was ~5 kcal/mol more favorable when they were anticorrelated because of the side-chain dipole moments.

In summary, the polar side chains had two conformations in the oxidized state but only one in the reduced state. For both the Asn and the His, the interaction energies between the positive χ_2 conformation and the cluster were very similar to the crystal structure but those of the negative χ_2 conformation were more positive (less favorable) by 1100 and 213 mV, respectively, thus resulting in more positive values of $-\Delta E/n\Im$. Moreover, the interaction energy of the negative χ_2 conformation was even more unfavorable in the reduced state because the attraction between the side chain and the redox site in the more highly charged reduced state was stronger so only the positive χ_2 conformation was observed. Thus, whereas the presence of the negative χ_2 conformation in the oxidized state led to large $-\Delta E/n\Im$ implying energetically favorable reduction, the reduction of this conformation is unfavorable and so a transition to the positive χ_2 conformation must occur before reduction. The free energy of reduction is thus much lower than the energy of reduction.

Because the expression for the free energy (Eq. 5) assumes a linear response, the linearity of the side-chain response to reduction was also explored by calculating $\xi^{(1)}_{-1,-2}$ given by Eq. 6 (Table 3). Previous results indicate that although the protein matrix of CpRr has both a permanent polarization that is present even when the redox site has no net charge as well as a contribution that responds by polarizing linearly with respect to the total redox site charge, the overall system appears more linear because the solvent has only a response contribution (37). The nonpolar residues, which included all the residues except Asn^8 in V8N and the triple mutant, and His^{44} in V44H and the triple mutant, generally had $\xi^{(1)}_{-1,-2} \approx 1/2$ except for Val^{44} where the numbers were too close to zero, thus indicating a permanent polarization contribution by the backbone dipoles of these residues. On the other hand, the polar Asn and His generally had $\xi^{(1)}_{-1,-2} \approx 1$, thus indicating these residues responded linearly to the reduction. The ratio of $\Delta G/\Delta E$ (Table 3) also provides an indication of the linearity, although the expression for the free energy given by Eq. 5 holds only for the linear regime. $\Delta G/\Delta E \approx 1/2$ did not hold for the nonpolar side chains, as expected when there is a nonlinear component to the response, whereas $\Delta G/\Delta E \approx 1/2$ for the polar side chains; i.e., Asn^8 in V8N and the triple mutant, and His^{44} in V44H and the triple mutant. Thus, Eq. 5 is reliable for Asn and His but not the nonpolar side chains. Of course, these values just indicate consistency with linear and nonlinear components, but do not prove either.

Because the side chains of these two residues had two conformations in the oxidized state and only one in the

TABLE 3 Nonlinearity calculated from MD simulations in CpRd wt and mutants

	8		41		44	
Protein	$\xi^{(1)}_{-1,-2}$	$\Delta G/\Delta E$	$\xi^{(1)}_{-1,-2}$	$\Delta G/\Delta E$	$\xi^{(1)}_{-1,-2}$	$\Delta G/\Delta E$
CpRd	0.60	0.74	0.53	0.88	—*	0.33
V8N	0.92	0.50	0.55	0.85	—*	0.18
L41A	0.61	0.74	0.59	0.78	—*	0.34
V44H	0.74	0.60	0.53	0.89	0.69	0.66
Triple	1.36	0.41	0.55	0.87	1.05	0.44

*Numbers are too close to zero.

reduced state, these side chains responded apparently linearly to the reduction by shifting the populations of the conformations, which have very different polarization energies. This shift in populations is necessary to get good agreement of the free energy from MD with the experimental reduction potentials. However, the backbone and side chains that do not rotate contribute to the permanent polarization around the redox center. Furthermore, as the two polar side chains did not appear here to be able to rotate in the reduced state, they might have only a permanent polarization contribution for a change from the reduced state to a super-reduced state. However, in the ferredoxins, the side chains did not rotate and thus contribute a permanent polarization energy (28). Interestingly, the ferredoxins utilize a 2-/3- couple whereas the HiPIPs and rubredoxins use a 1-/2- couple, indicating that shifting conformation populations may saturate for clusters of charge 2- so that the 2-/3- couple may tend to be nonlinear. Finally, the anticorrelation of the Asn and His side chain conformation will tend to keep the energy difference between the oxidized and reduced state more constant, which is important when considering the effects of the conformations on electron transfer rates.

MD also suggests that differences in water penetration may play a role here. The MD simulations show an increase in water near the redox site upon reduction (Table 4) as seen in earlier simulations (17,54) and later in crystal structures (15,16). For most of the simulations, the number of waters within 6 Å of the iron is ~1 for the oxidized state and 2–3 for the reduced state. The CpRd L41A and triple mutant show slight increases in water penetration relative to wt and may be responsible for the 50 mV increase in E° between L41A and wt. Even though both the SCSA of the monomer and the MD of the CpRd L41A mutant show a slight increase in the solvent accessibility, the natural form of rubrerythrin is a homodimer, and the interface between the hemerythrin domain and the rubredoxin domain completely blocks solvent accessibility to the area of the alanine, as evident by nearly 0 $Å^2$ SCSA of the homodimer. This means that the alanine determinant cannot provide a significant increase to the reduction potential of the rubredoxinlike domain of DvRr over that of CpRd through an increase in solvent accessibility to bulk water. Because all of the simulations show an increase in the number of waters near the redox site upon reduction, as was also observed crystallographically in the wt (16), the dimerization of rubrerythrin may actually lead to a decrease in E° in which the water penetration cannot occur because the redox site is blocked by the other monomer. Thus, although rubredoxin has a water gate allowing entry of water (15–17), rubrerythrin may have a water gate that is permanently closed in the homodimer that traps a water inside.

TABLE 4 Numbers of waters within 6 Å of the iron of the redox site in MD simulations

	Number of waters	
Protein	Oxidized state	Reduced state
CpRd	0.8	2.4
Cp V8N	0.9	1.8
Cp L41A	1.3	2.8
Cp V44H	0.7	1.8
Cp Triple	1.1	3.0

Overall, the free energy differences from the molecular dynamics between the wt and mutants in CpRd were in good agreement with experimental differences between CpRd and DvRr for the polar side chains. However, the free energies for backbone contributions calculated using Eq. 5 are less accurate because they are nonlinear (i.e., have a permanent contribution). Thus, in cases where backbone shifts are important such as in previous studies of rubredoxins (12) and the ferredoxins (28), energy calculations of multiple high-resolution crystal structures showing systematic differences in their sequences (26) are likely to be more reliable.

CONCLUSIONS

The work presented here provides insights into the increased reduction potential of the rubredoxin domain of rubrerythrin over that of rubredoxin. The increased reduction potential appears to come mainly from the addition of the polar groups of Asn^8 (160, DvRr numbering) and His^{44} (179) near the redox center. Also, Ala^{41} (176) may be less of a contributor to the increased reduction potential because solvent accessibility is negligible in the homodimer, although it may be important for the CpRd V41A mutant. Overall, these results along with previous studies of the rubredoxins (12) and the ferredoxins (28) show that our method of bioinformatics sequence and electrostatic crystal structural analysis (25,26) is useful for identifying sequence determinants between homologous proteins where there are many nonidentical residues. In addition, the differences in reduction potentials predicted by free energies calculated from MD simulations of mutants are in good agreement with experimental values. In other words, although the simple analyses of crystal structures are useful in identifying sequence determinants of reduction potentials, MD simulations are useful in predicting the changes in reduction potentials due to mutations of these sequence determinants.

More generally, the simulations indicate that different elements of the protein can respond differently to the change in charge of the redox sites. Previous results indicate that whereas the protein matrix has both a large permanent polarization as well as a linear response, the overall system demonstrates a linear response due to the solvent (37). Here, individual residues are shown to have anywhere from a permanent polarization to a linear response. Specifically, the Asn and His exhibit a linear response via the interesting mechanism of changing the relative populations of two side-chain conformations in the oxidized versus reduced states.

SUPPORTING MATERIAL

Two figures are available at http://www.biophysj.org/biophysj/supplemental/S0006-3495(09)01729-9.

This work was supported by a grant from the National Institutes of Health (No. GM45303). Computer time was provided by the National Partnership for Advanced Computational Infrastructure at the Texas Advanced Computing Center and the TeraGrid under the National Science Foundation cooperative agreement No. MCB990010. Resources from the William G. McGowan Foundation are gratefully acknowledged. In addition, this research was supported in part by the Intramural Research Program of the National Heart, Lung, and Blood Institute, National Institutes of Health (Laboratory of Computational Biology).

The views and conclusions contained in this document are those of the authors and should not be interpreted as necessarily representing the official policies or endorsements, either expressed or implied, of the U.S. government.

REFERENCES

1. Johnson, D. C., D. R. Dean, …, M. K. Johnson. 2005. Structure, function, and formation of biological iron-sulfur clusters. *Annu. Rev. Biochem.* 74:247–281.
2. Meyer, J. 2008. Iron-sulfur protein folds, iron-sulfur chemistry, and evolution. *J. Biol. Inorg. Chem.* 13:157–170.
3. Beinert, H., J. Meyer, and R. Lill. 2004. Iron-sulfur proteins. *In* Encyclopedia of Biological Chemistry, Vol. 2. Elsevier, Amsterdam, The Netherlands., 482–489.
4. Cammack, R. 1992. Iron-sulfur cluster in enzymes: themes and variations. *Adv. Inorg. Chem.* 38:281–322.
5. Beinert, H., R. H. Holm, and E. Münck. 1997. Iron-sulfur clusters: nature's modular, multipurpose structures. *Science*. 277:653–659.
6. LeGall, J., B. C. Prickril, …, B. H. Huynh. 1988. Isolation and characterization of rubrerythrin, a non-heme iron protein from *Desulfovibrio vulgaris* that contains rubredoxin centers and a hemerythrin-binuclear iron cluster. *Biochemistry*. 27:1636–1642.
7. Alban, P. S., D. L. Popham, …, N. R. Krieg. 1998. Identification of a gene for a rubrerythrin/nigerythrin-like protein in *Spirillum volutans* by using amino acid sequence data from mass spectrometry and NH_2-terminal sequencing. *J. Appl. Microbiol.* 85:875–882.
8. Coulter, E. D., and D. M. J. Kurtz, Jr. 2001. A role for rubredoxin in oxidative stress protection in *Desulfovibrio vulgaris*: catalytic electron transfer to rubrerythrin and two-iron superoxide reductase. *Arch. Biochem. Biophys.* 394:76–86.
9. Lumppio, H. L., N. V. Shenvi, …, D. M. Kurtz, Jr. 2001. Rubrerythrin and rubredoxin oxidoreductase in *Desulfovibrio vulgaris*: a novel oxidative stress protection system. *J. Bacteriol.* 183:101–108.
10. deMaré, F., D. M. J. Kurtz, Jr., and P. Nordlund. 1996. The structure of *Desulfovibrio vulgaris* rubrerythrin reveals a unique combination of rubredoxin-like FeS_4 and ferritin-like diiron domains. *Nat. Struct. Biol.* 3:539–546.
11. Messerschmidt, A., R. Huber, K. Wieghardt, and T. Poulos, editors. 2001. Handbook of Metalloproteins. Wiley, New York.
12. Swartz, P. D., B. W. Beck, and T. Ichiye. 1996. Structural origins of redox potentials in Fe-S proteins: electrostatic potentials of crystal structures. *Biophys. J.* 71:2958–2969.
13. Eidsness, M. K., A. E. Burden, …, C. Kang. 1999. Modulation of the redox potential of the $Fe(SCys)_4$ site in rubredoxin by the orientation of a peptide dipole. *Biochemistry*. 38:14803–14809.
14. Ergenekan, C. E., D. Thomas, …, T. Ichiye. 2003. Prediction of reduction potential changes in rubredoxin: a molecular mechanics approach. *Biophys. J.* 85:2818–2829.
15. Park, I. Y., B. Youn, …, C. Kang. 2004. The unique hydrogen bonded water in the reduced form of *Clostridium pasteurianum* rubredoxin and its possible role in electron transfer. *J. Biol. Inorg. Chem.* 9:423–428.
16. Min, T., C. E. Ergenekan, …, C. Kang. 2001. Leucine 41 is a gate for water entry in the reduction of *Clostridium pasteurianum* rubredoxin. *Protein Sci.* 10:613–621.
17. Yelle, R. B., N.-S. Park, and T. Ichiye. 1995. Molecular dynamics simulations of rubredoxin from *Clostridium pasteurianum*: changes in structure and electrostatic potential during redox reactions. *Prot. Struct. Funct. Gen.* 22:154–167.
18. Stephens, P. J., D. R. Jollie, and A. Warshel. 1996. Protein control of redox potentials of iron-sulfur proteins. *Chem. Rev.* 96:2491–2514.
19. Mouesca, J.-M., J. L. Chen, …, D. A. Case. 1994. Density functional/Poisson-Boltzmann calculations of redox potentials for iron-sulfur clusters. *J. Am. Chem. Soc.* 116:11898–11914.
20. Torres, R. A., T. Lovell, …, D. A. Case. 2003. Density functional and reduction potential calculations of Fe_4S_4 clusters. *J. Am. Chem. Soc.* 125:1923–1936.
21. Sulpizi, M., S. Raugei, …, M. Sprik. 2007. Calculation of redox properties: understanding short- and long-range effects in rubredoxin. *J. Phys. Chem. B.* 111:3969–3976.
22. Zeng, Q., E. T. Smith, …, R. A. Scott. 1996. Protein determinants of metal site reduction potentials. Site directed mutagenesis studies of *Clostridium pasteurianum* rubredoxin. *Inorg. Chim. Acta*. 242:245–251.
23. Gleason, F. K. 1992. Mutation of conserved residues in *Escherichia coli* thioredoxin: effects on stability and function. *Protein Sci.* 1:609–616.
24. Shen, B., D. R. Jollie, …, B. K. Burgess. 1994. *Azotobacter vinelandii* ferredoxin I. Alteration of individual surface charges and the $[4FE\text{-}4S]^{2+/+}$ cluster reduction potential. *J. Biol. Chem.* 269:8564–8575.
25. Ichiye, T. 1996. Solvent free energy curves for electron transfer: a nonlinear solvent response model. *J. Chem. Phys.* 104:7561–7571.
26. Ichiye, T. 2001. Simulations of electron transfer proteins. *In* Computational Biochemistry and Biophysics. O. M. Becker, A. D. MacKerell, Jr., B. Roux, and M. Watanabe, editors. Marcel Dekker, New York, NY. 393–415.
27. Xiao, Z., M. J. Maher, …, A. G. Wedd. 2000. Mutation of the surface valine residues 8 and 44 in the rubredoxin from *Clostridium pasteurianum*: solvent access versus structural changes as determinants of reversible potential. *J. Biol. Inorg. Chem.* 5:75–84.
28. Beck, B. W., Q. Xie, and T. Ichiye. 2001. Sequence determination of reduction potentials by cysteinyl hydrogen bonds and peptide pipoles in [4Fe-4S] ferredoxins. *Biophys. J.* 81:601–613.
29. Iismaa, S. E., A. E. Vázquez, …, B. K. Burgess. 1991. Site-directed mutagenesis of *Azotobacter vinelandii* ferredoxin I. Changes in [4Fe-4S] cluster reduction potential and reactivity. *J. Biol. Chem.* 266:21563–21571.
30. Brereton, P. S., M. F. J. M. Verhagen, …, M. W. W. Adams. 1998. Effect of iron-sulfur cluster environment in modulating the thermodynamic properties and biological function of ferredoxin from *Pyrococcus furiosus*. *Biochemistry*. 37:7351–7362.
31. Kümmerle, R., J. Gaillard, …, J. M. Moulis. 2001. Intramolecular electron transfer in [4Fe-4S] proteins: estimates of the reorganization energy and electronic coupling in *Chromatium vinosum* ferredoxin. *J. Biol. Inorg. Chem.* 6:446–451.
32. Tan, M.-L., C.-H. Kang, and T. Ichiye. 2006. The role of backbone stability near Ala^{44} in the high reduction potential class of rubredoxins. *Prot. Struct. Funct. Bioinform.* 62:708–714.
33. Ichiye, T., and M. Karplus. 1988. Anisotropy and anharmonicity of atomic fluctuations in proteins: implications for x-ray analysis. *Biochemistry*. 27:3487–3497.
34. LeBard, D. N., and D. V. Matyushov. 2008. Glassy protein dynamics and gigantic solvent reorganization energy of plastocyanin. *J. Phys. Chem. B.* 112:5218–5227.
35. Tan, M.-L., E. A. Dolan, and T. Ichiye. 2004. Understanding intramolecular electron transfer in ferredoxin: a molecular dynamics study. *J. Phys. Chem. B.* 108:20435–20441.
36. Muegge, I., P. X. Qi, …, A. Warshel. 1997. The reorganization energy of cytochrome *c* revisited. *J. Phys. Chem. A.* 101:825–836.

37. Dolan, E. A., R. B. Yelle, …, T. Ichiye. 2004. Protein control of electron transfer rates via polarization: molecular dynamics studies of rubredoxin. *Biophys. J.* 86:2030–2036.

38. Warshel, A., P. K. Sharma, …, M. H. Olsson. 2006. Electrostatic basis for enzyme catalysis. *Chem. Rev.* 106:3210–3235.

39. Jin, S., D. M. Kurtz, Jr., …, B. C. Wang. 2002. X-ray crystal structures of reduced rubrerythrin and its azide adduct: a structure-based mechanism for a non-heme diiron peroxidase. *J. Am. Chem. Soc.* 124: 9845–9855.

40. Bernstein, F. C., T. F. Koetzle, …, M. Tasumi. 1977. The Protein Data Bank: a computer-based archival file for macromolecular structures. *J. Mol. Biol.* 112:535–542.

41. Brooks, B. R., R. E. Bruccoleri, …, M. Karplus. 1983. CHARMM: a program for macromolecular energy, minimization, and dynamics calculations. *J. Comput. Chem.* 4:187–217.

42. Sieker, L. C., M. Holmes, …, R. E. Stenkamp. 2000. The 1.9 Å crystal structure of the ''as isolated'' rubrerythrin from *Desulfovibrio vulgaris*: some surprising results. *J. Biol. Inorg. Chem.* 5:505–513.

43. Altschul, S. F., W. Gish, …, D. J. Lipman. 1990. Basic local alignment search tool. *J. Mol. Biol.* 215:403–410.

44. Boeckmann, B., A. Bairoch, …, M. Schneider. 2003. The SWISS-PROT protein knowledgebase and its supplement TrEMBL in 2003. *Nucleic Acids Res.* 31:365–370.

45. Watenpaugh, K. D., L. C. Sieker, and L. H. Jensen. 1980. Crystallographic refinement of rubredoxin at 1×2 Å degrees resolution. *J. Mol. Biol.* 138:615–633.

46. Jorgensen, W. L. 1981. Transferable intermolecular potential functions for water, alcohols, and ethers. Application to liquid water. *J. Am. Chem. Soc.* 103:335–340.

47. Rychaert, J. P., G. Ciccotti, and H. J. C. Berendsen. 1977. Numerical integration of the Cartesian equation of motion of a system with constraints: molecular dynamics of *n*-alkanes. *J. Comput. Phys.* 23:327–341.

48. Steinbach, P. J., and B. R. Brooks. 1994. New spherical-cutoff methods for long-range forces in macromolecular simulation. *J. Comput. Chem.* 15:667–683.

49. MSI. 1986–1998. QUANTA98. Ver. 98.1111. Biosym/MSI, San Diego, CA.

50. Tateyama, Y., J. Blumberger, …, I. Tavernelli. 2005. Density-functional molecular-dynamics study of the redox reactions of two anionic, aqueous transition-metal complexes. *J. Chem. Phys.* 122:234505.

51. King, G., and A. Warshel. 1990. Investigation of the free energy functions for electron transfer reactions. *J. Chem. Phys.* 93:8682–8692.

52. Böttcher, C. J. F. 1973. Theory of Electric Polarization. Elsevier Scientific, Amsterdam, The Netherlands.

53. Lee, B., and F. M. Richards. 1971. The interpretation of protein structures: estimation of static accessibility. *J. Mol. Biol.* 55:379–400.

54. Swartz, P. D., and T. Ichiye. 1996. Temperature dependence of the redox potential of rubredoxin from *Pyrococcus furiosus:* a molecular dynamics study. *Biochemistry.* 35:13772–13779.